Scientific Reports

https://doi.org/10.1038/s41598-026-50591-2

Article in Press

Design and optimization of double semi-cylindrical plasmonic nanostructures for enhanced light harvesting in ultrathin CIGS solar cells

Received: 8 October 2025

Accepted: 22 April 2026

Published online: 25 April 2026

Cite this article as: Bahador H., Jangjoy A. & Nilghaz A. Design and optimization of double semi-cylindrical plasmonic nanostructures for enhanced light harvesting in ultrathin CIGS solar cells. *Sci Rep* (2026). https://doi.org/10.1038/s41598-026-50591-2

Hamid Bahador, Abolfazl Jangjoy & Azadeh Nilghaz

We are providing an unedited version of this manuscript to give early access to its findings. Before final publication, the manuscript will undergo further editing. Please note there may be errors present which affect the content, and all legal disclaimers apply.

If this paper is publishing under a Transparent Peer Review model then Peer Review reports will publish with the final article.

ARTICLE IN PRESS

© The Author(s) 2026. **Open Access** This article is licensed under a Creative Commons Attribution-NonCommercial-NoDerivatives 4.0 International License, which permits any non-commercial use, sharing, distribution and reproduction in any medium or format, as long as you give appropriate credit to the original author(s) and the source, provide a link to the Creative Commons licence, and indicate if you modified the licensed material. You do not have permission under this licence to share adapted material derived from this article or parts of it. The images or other third party material in this article are included in the article's Creative Commons licence, unless indicated otherwise in a credit line to the material. If material is not included in the article's Creative Commons licence and your intended use is not permitted by statutory regulation or exceeds the permitted use, you will need to obtain permission directly from the copyright holder. To view a copy of this licence, visit http://creativecommons.org/licenses/by-nc-nd/4.0/.

ARTICLE IN PRESS

Design and optimization of double semi-cylindrical plasmonic nanostructures for enhanced light harvesting in ultrathin CIGS solar cells

Hamid Bahador[1, *], Abolfazl Jangjoy[1], Azadeh Nilghaz[2]

[1] Department of Electrical and Computer Engineering, University of Mohaghegh Ardabili, Ardabil, Iran

[2] Drug Delivery, Disposition, and Dynamics, Monash University, Parkville, VIC 3052, Australia

*Corresponding author: hamid.bahador@uma.ac.ir

Abstract:
This work presents a theoretical study on ultrathin Cu(In_xGa1-x)Se_2 (CIGS) solar cells with an absorber thickness of only 200 nm, enhanced by plasmonic nanoparticles (NPs). The inherent trade-off reduced absorber thickness, and sufficient light absorption was addressed by investigating metallic nanoparticles of silver (Ag), gold (Au), aluminum (Al), nickel (Ni), and titanium (Ti) in spherical and cylindrical configurations. Building on this approach, a single semi-cylindrical geometry was introduced to minimize optical losses, and the inter-particle spacing was systematically optimized to maximize light trapping. Three-dimensional finite difference time domain (3D-FDTD) simulations revealed that the interaction between coupled NPs strengthens both the localized fields around the NPs and the scattered fields within the absorber, leading to more efficient carrier generation. In the optimized case, the semi-cylindrical double NPs (DNP) structure exhibited a 29% higher near-field intensity at the resonance wavelength of 731 nm compared with the single half-cylindrical design, highlighting the crucial role of plasmonic coupling. As a result, the short-circuit current density (J_{SC}) increased from 22.50 (mA/cm²) to 31.12 mA/cm², representing an increase of 38.3%. In addition, the power conversion efficiency (PCE) increased by 40.3%, from 12.97% to 18.20%. These findings demonstrate that carefully engineered plasmonic nanostructures can substantially enhance the performance of next-generation thin-film CIGS photovoltaic devices.

Keywords: CIGS solar cell, ultrathin absorber, light trapping, efficiency enhancement

1. Introduction

Fossil fuels have long been the dominant source of electricity generation, yet their environmental impacts and limited availability have accelerated the transition toward renewable energy technologies. In this context, clean and sustainable energy sources have become an urgent priority. Solar

ARTICLE IN PRESS

photovoltaics (PV) are particularly attractive due to the abundance of sunlight, scalability, and silent, pollution-free operation. While crystalline silicon continues to dominate the commercial PV market, thin-film technologies offer lower fabrication costs, lightweight, and additional design flexibility [1, 2]. Among them, copper indium gallium selenide (CIGS) solar cells stand out as a leading candidate owing to their unique optoelectronic properties, including a high absorption coefficient (~10^5 cm^{-1}), a tunable direct bandgap ranging from 1.0 eV to 1.7 eV, through precise control of the gallium-to-indium ratio (X = [Ga]/([Ga]+[In])), and excellent long-term stability. These advantages have enabled CIGS solar cells to achieve record efficiencies exceeding 23%, positioning them as one of the most promising thin-film photovoltaic technologies [3, 4].

However, reliance on scarce and expensive elements such as indium and gallium poses challenges for cost-effective, large-scale deployment. A widely adopted solution is to reduce the absorber thickness below 500 nm, which lowers material consumption and production cost [5, 6]. Nevertheless, such ultrathin absorbers suffer from incomplete photon absorption, resulting in reduced short-circuit current densities and efficiency losses, thereby falling well short of the Shockley–Queisser limit. This trade-off between material economy and optical performance represents a significant bottleneck for ultrathin CIGS photovoltaics. Several light management strategies, such as reflective back contacts, anti-reflective coatings, and passivation layers, have been explored to address this challenge. However, their impact remains insufficient to fully compensate for the absorption losses [7-9].

In recent years, plasmonic nanostructures have emerged as a more powerful alternative. When free electrons in metallic NPs interact with incident light, localized surface plasmon resonances (LSPR) are excited, leading to substantial near-field enhancement and efficient far-field scattering. These effects extend the optical path length within the absorber beyond its physical thickness, thereby improving photon absorption and carrier generation [10, 11]. The effectiveness of plasmonic enhancement is governed not only by the intrinsic properties of the chosen metal but also by the geometry, dimensions, and spatial arrangement of the NPs [12]. In addition to these theoretical considerations, recent experimental and numerical studies have confirmed that plasmonic nanoparticles can effectively enhance optical absorption in thin-film photovoltaic devices through localized surface plasmon resonance and near-field enhancement mechanisms. Experimental demonstrations in thin-film and GaAs-based solar cells have shown that metallic nanoparticles can improve optical absorption and external quantum efficiency by enhancing forward scattering and electromagnetic field localization near the absorber interface [13]. More recent investigations further reveal that the plasmonic response is strongly influenced by nanoparticle size, interparticle spacing, and the surrounding dielectric environment, which determine resonance position, field confinement, and absorption bandwidth [14-16]. These results highlight the importance of geometrical optimization and nanoparticle coupling in achieving broadband absorption enhancement in ultrathin

ARTICLE IN PRESS

photovoltaic absorbers. In parallel with experimental developments, numerical electromagnetic approaches, particularly the FDTD method, have become widely adopted for analyzing plasmonic effects in photovoltaic structures due to their capability to rigorously solve Maxwell's equations and accurately capture nanoscale light–matter interactions. Recent FDTD-based studies on plasmon-enhanced thin-film solar cells have demonstrated that embedded nanoparticle configurations and coupled nanostructures can significantly modify absorption spectra and carrier generation profiles, thereby providing reliable design guidelines before experimental realization [14, 15].

Noble metals such as Ag and Au have traditionally dominated this field because of their strong plasmonic resonances, high free-electron densities, and broadband optical response [17]. Nevertheless, alternative metals such as Al and copper (Cu) are also of great interest, primarily because of their lower cost and higher abundance compared with Ag and Au, making them attractive for scalable photovoltaic applications despite their higher intrinsic losses [18, 19]. However, most studies have been limited to relatively simple shapes, spheres, cylinders, or hemispheres, where the enhancement arises from isolated resonances [7, 19, 20]. By contrast, more sophisticated or coupled nanostructures can induce hybridized plasmonic modes through inter-particle interactions, leading to stronger, spatially confined fields and broader spectral coverage [21]. Exploring such coupling effects, therefore, represents a promising pathway to overcome the absorption limitations of ultrathin CIGS devices and to push their efficiency beyond what is achievable with conventional nanoparticle designs, all while maintaining low material consumption.

In light of these considerations, this work introduces a novel plasmonic design based on DNP integrated into ultrathin CIGS solar cells. The motivation for this geometry lies in its ability to exploit strong plasmonic coupling between adjacent nanoparticles, thereby generating intense near-field hot spots and enhanced far-field scattering that cannot be achieved with single or conventional shapes. Using comprehensive 3D-FDTD simulations, we systematically evaluate the role of nanoparticle material (Ag, Au, Al, Ni, and Ti), geometric configuration, inter-particle spacing, and oxidation on light absorption and charge-carrier generation. Our findings demonstrate that the optimized DNP configuration significantly boosts the J_{SC} and overall PCE compared with traditional designs. This study highlights a promising pathway toward high-performance, cost-effective ultrathin CIGS photovoltaics, advancing the scalability of next-generation solar technologies.

2. Structure Design and Simulation Method

The simulated architecture of the ultrathin CIGS solar cell is illustrated in Figure 1a. The device adopts a multilayer configuration representative of

ARTICLE IN PRESS

state-of-the-art thin-film photovoltaics. At the bottom, a 10 nm molybdenum (Mo) layer is employed as the back contact. For simplicity in the simulation, the Mo back junction was set to 10 nm, mainly to focus on the effects of the plasmonic nanoparticles and the ultrathin absorber layer. While in practical CIGS devices, the Mo layer is usually extended beyond 400 nm to ensure low sheet resistance and strong back reflection, the choice of a 10 nm layer in this study was made with the aim of minimizing computational complexity and isolating the influence of the plasmonic design. This thinner layer introduces resistive and optical limitations, but it does not significantly affect the main goal of optimizing the nanoparticle configuration. Mo is widely used in CIGS devices due to its high conductivity, strong adhesion to the glass substrate, and the formation of a thin $MoSe_2$ interfacial layer during selenization, which ensures a low-resistance ohmic contact with the absorber [22]. Above this, the 200 nm $Cu(In_xGa1\text{-}x)Se_2$ (CIGS) absorber is deposited with a gallium concentration value equal to 0.4 (X = 0.4). This composition corresponds to a direct bandgap of approximately 1.26 eV, which is well-suited for efficient solar energy conversion [23]. It combines strong light absorption with effective carrier collection, while also limiting reliance on scarce gallium.

To optimize charge separation at the junction, a 50 nm cadmium sulfide (CdS) buffer layer is added. The optimal radius (R = 50 nm) and gap (d = 40 nm) values in Table 1 were selected through 3D-FDTD simulations aimed at maximizing light absorption and short-circuit current density (J_{SC}) within the CIGS absorber. These values provided the best trade-off between enhanced near-field intensity and minimized parasitic absorption losses. Although the configuration in Figure 2(c) with R = 55 nm and d = 30 nm shows a slight improvement in J_{SC}, it results in higher parasitic absorption and weaker plasmonic coupling, making the R = 50 nm and d = 40 nm configuration more efficient overall. CdS forms a favorable heterojunction with CIGS, passivates interface defects, and enhances carrier selectivity by suppressing electron–hole recombination at the absorber surface [24]. On top of the buffer, a 30 nm zinc oxide (ZnO) layer acts as the window layer, providing high optical transparency across the visible spectrum together with moderate conductivity. Finally, an 80 nm aluminum-doped zinc oxide (AZO) layer is deposited as the transparent conductive oxide

ARTICLE IN PRESS

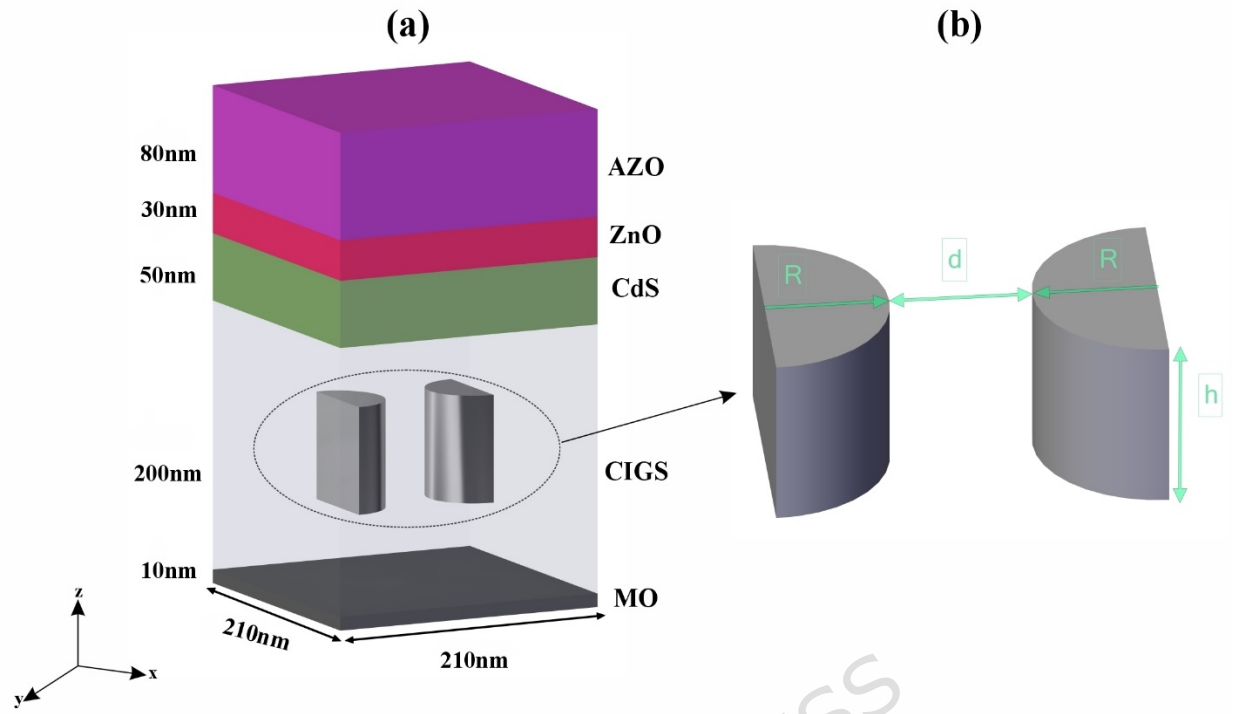

Figure 1. (a) Three-dimensional schematic of the simulated ultrathin CIGS solar cell architecture. (b) Proposed DNP configuration incorporated into the CIGS absorber layer.

(TCO) and front electrode. AZO is selected for its high transparency (T>86%), good lateral conductivity, and long-term stability, while being more cost-effective and abundant than the widely used indium tin oxide (ITO) [25]. The lateral dimensions in the x and y directions were set to 210 nm × 210 nm, corresponding to the unit cell of the periodic nanoparticle array. In this way, a single unit cell is simulated with periodic boundary conditions, which accurately represents the behavior of an extended array without the need to model the entire device. A summary of the complete layer stack and material parameters is provided in Table 1.

Table 1. Simulation parameters and boundary conditions.

Parameter	Description	Material	Thickness/length(nm)
L_x, L_y	Period of the unit cell	-	210
$h\text{-}_{AZO}$	Height of ARC	AZO	80
$h\text{-}_{ZnO}$	Height of secondary buffer	ZnO	30
$h\text{-}_{CdS}$	Height of buffer	CdS	50
$h\text{-}_{CIGS}$	Height of absorber	CIGS	200
$h\text{-}_{Mo}$	Height of back contact	Mo	10
R	Optimal radius of NPs	Ag, Al, Au, Ni, Ti	50
d	Optimal gap of the DNP	-	40
h	Height of the NPs	Ag, Al, Au, Ni, Ti	120

ARTICLE IN PRESS

S	Thickness of metal oxide shell	Ag_2O, Al_2O_3, NiO, TiO_2	3

Directions	Boundary conditions
x and y directions	Periodic boundary conditions
z direction	Perfectly matched layer

All optical simulations were performed using the 3D-FDTD method, implemented in the Lumerical FDTD Solutions package. To ensure the numerical conservation of energy, we confirmed that the sum of total reflection, transmission, and absorption equals 1 across all wavelengths in our simulations. This validation ensures that energy is conserved within the optical model. When estimating the short-circuit current density (J_{sc}), both reflection and transmission are inherently accounted for. The J_{sc} is determined based on the absorbed light within the CIGS layer, with the reflection and transmission losses factored into the absorption enhancement calculations, which directly influence carrier generation. The structure was illuminated by a normally incident plane-wave source propagating along the negative z-axis. The excitation spectrum was set to 300–984 nm, covering the relevant portion of the AM1.5G solar spectrum and fully encompassing the absorption edge of CIGS with a Ga molar concentration (X) equal to 0.4. To emulate an infinite nanoparticle array, periodic boundary conditions (PBC) were applied in the lateral x–y directions, while perfectly matched layers (PML) were imposed along the z-axis to eliminate spurious reflections [26]. The optical constants (n and k) of the CIGS absorber were obtained from experimental measurements [23], while those for the remaining layers and metallic NPs were taken from the Palik dataset as implemented in the software material library [27].

To improve the optical response of the ultrathin CIGS solar cell, we first investigated spherical and cylindrical nanoparticles of optimized size. However, these geometries exhibited increased optical losses, which motivated the introduction of single and double semi-cylindrical NPs. As shown in Fig. 1b, the DNP design is characterized by three key parameters: the nanoparticle radius (R), height (h), and interparticle gap (d). In the case of the DNP configuration, the period was kept constant at 210 nm for consistency in the simulation. However, this period results in a reduced available volume for each NP in the DNP design compared to the SNP configuration. Although the volume per nanoparticle is technically smaller in the DNP arrangement, the comparison remains rational because the primary goal was to examine the effect of plasmonic coupling between adjacent nanoparticles. This coupling enhances light trapping and absorption. To avoid the formation of shunt paths and prevent direct electrical contact with neighboring layers, the nanoparticle height was fixed at 120 nm. With this constraint, the radius and interparticle gap were systematically varied to determine the conditions that maximize optical absorption and overall device efficiency. The optimization process was guided by the primary goal of

ARTICLE IN PRESS

maximizing the J_{SC} generated exclusively from photon absorption in the CIGS absorber. At each step, parasitic absorption within the metallic nanoparticles was carefully monitored to ensure the best trade-off between useful absorption enhancement and unwanted optical dissipation. To evaluate the long-term stability of the plasmonic configurations, complementary simulations were conducted by surrounding each NP with a 3 nm uniform native oxide shell. The oxides considered were Ag_2O for Ag [28], Al_2O_3 for Al [29], NiO for Ni [30], and TiO_2 for Ti [31], while Au was modeled without an oxide coating due to its intrinsic resistance to oxidation.

In the FDTD framework, oxidation is not modeled as a chemical or time-dependent process but as an effective optical modification of the nanoparticle environment. The oxidized nanoparticles were therefore represented using a core–shell configuration, where the metallic core is surrounded by a thin dielectric oxide layer with wavelength-dependent optical properties. The influence of oxidation was evaluated by comparing the absorption spectra and optical generation results of oxidized and non-oxidized configurations under identical simulation conditions. To quantitatively evaluate the optical and electrical performance of the proposed structures, a set of standard equations was employed. The optical response is first described in terms of the absorbed power density (P_{abs}) at any point inside the device, given by Equation (1).

$$P_{abs} = -\,real(\tilde{N}.\vec{P}) = -\frac{1}{2}\omega\varepsilon_0 |E(r,\omega)|^2 \,\mathrm{Im}(\varepsilon(r,\omega)) \quad (1)$$

where ω is the angular frequency, ε_0 is the vacuum permittivity, E is the local electric field intensity, and Im(ε(r, ω)) represents the imaginary part of the relative permittivity of the medium. Beyond the absorption spectrum, the absorption enhancement factor was introduced to quantitatively assess the improvement in photon absorption induced by plasmonic nanoparticles. This factor directly compares the absorbed power in the Ag and Al NPs demonstrate significantly layer with and without nanoparticles, and is expressed by Equation (2) [32].

$$Abs\text{-}enhancement = \frac{P_{abs,NP}(/)}{P_{abs,Bare}(/)} \quad (2)$$

where $P_{abs,NP}$ represents the absorbed power in the CIGS layer in the presence of NPs, and $P_{abs,bare}$
denotes the absorbed power in the corresponding bare structure without NPs. When light absorption is enhanced, more electron–hole pairs are generated inside the CIGS absorber. Assuming that every absorbed photon contributes to carrier generation (unity internal quantum efficiency), the

ARTICLE IN PRESS

optical generation rate (G) can be determined by dividing the absorbed optical power by the photon energy, as expressed in Equation (3).

$$G = \frac{P_{abs}}{photonenergy} = -\frac{\omega}{2}\left|E(r,\omega)\right|^2 \{\varepsilon(r,\omega)\} \quad (3)$$

The term $|E(r,\omega)|^2$ captures the intensity of the local electric field at a given position. The generation rate is particularly useful because it not only provides a numerical measure of how efficiently photons are converted into carriers, but also allows us to visualize where inside the device this useful absorption occurs. In other words, the optical generation rate acts as a roadmap of where and how effectively photons are absorbed within the device. This spatially resolved information provides the foundation for calculating one of the most critical photovoltaic parameters, J_{SC}. As a direct measure of the number of photo-generated charge carriers that can be extracted under illumination, J_{SC} is obtained by integrating the product of the device absorption spectrum and the solar photon flux over the active wavelength range, as expressed in Equation (4).

$$J_{sc}(\lambda) = e\int_{300}^{984} \frac{\lambda}{hc}\frac{P_{abs}(\lambda)}{P_{in}(\lambda)} I_{AM1.5}(\lambda)\, d\lambda \quad (4)$$

Here, e is the electron charge (1.6×10^{-19} C), h is Planck's constant (4.1356×10^{-15} eV·s), c is the speed of light in vacuum (3×10^{8} m/s), P_{in} is the incident solar power density under AM1.5G conditions (100 mW/cm²), and $I_{AM1.5}(\lambda)$ denotes the spectral photon flux. In practical solar cell operation, the absorbed optical power varies with wavelength due to the spectral distribution of the incident solar radiation. Therefore, in addition to evaluating the wavelength-dependent absorbed power obtained from the FDTD simulations, a broadband optical metric is required to describe the overall absorption performance under realistic solar illumination conditions. For this purpose, the spectral absorption rate (SAR) is introduced as a solar-spectrum-weighted average absorbed power. The SAR is defined as [16, 33]:

$$SAR(\lambda) = \frac{\int P_{abs}(\lambda) I_{AM1.5}(\lambda)\, d(\lambda)}{\int I_{AM1.5}(\lambda)\, d(\lambda)} \quad (5)$$

where $P_{abs}(\lambda)$ represents the absorbed optical power in the CIGS absorber layer as a function of wavelength and $I_{AM1.5}(\lambda)$ denotes the spectral solar irradiance under standard AM1.5G illumination conditions. This formulation provides a quantitative measure of broadband optical absorption and enables consistent comparison of different nanoparticle configurations under realistic solar excitation. In addition to J_{SC} , two other photovoltaic parameters, namely the open-circuit voltage (V_{OC}) and the fill factor (FF), were

ARTICLE IN PRESS

determined using the standard single-diode model. The V_{OC}, which provides insight into carrier recombination within the absorber, is calculated as:

$$V_{oc} = 25.9 \ln\left(\frac{J_{sc}}{J_0} + 1\right) \quad (6)$$

where V_T is the thermal voltage (~25.9 mV at room temperature), and J_0 is the dark saturation current density. In this work, J_0 was taken as 7.2×10^{-11} A/cm^2, consistent with experimental values reported for CIGS with a Ga concentration of X=0.4 [23]. The fill factor (FF), which reflects the squareness of the J–V characteristic curve and thus the efficiency of power extraction, can be approximated by the following Equation.

$$FF = \frac{\frac{V_{oc}}{25.9} + \ln\left(\frac{V_{oc}}{25.9} + 0.72\right)}{\frac{V_{oc}}{25.9} + 1} \quad (7)$$

Combining these three quantities, J_{SC}, V_{OC}, and FF, yields the PCE, the ultimate figure of merit that describes the cell's ability to convert incident sunlight into electrical power.

$$PCE = \frac{J_{sc} V_{oc} FF}{P_{in}} \quad (8)$$

It is important to emphasize that both V_{OC} and FF are strongly influenced by recombination dynamics inside the absorber and at the interfaces. To provide a holistic view of the device performance, the complete J–V curve was simulated. This curve is obtained by numerically solving the single-diode equation, which accounts for both recombination and parasitic losses, as given in Equation (9).

$$J = J_{sc} - J_0\left(e^{(qV/(nkT))} - 1\right) - (V/r_{sh}) \quad (9)$$

Here, n is the diode ideality factor, k_T is the thermal energy, and r_{sh} is the shunt resistance. Finally, the value of the shunt resistance is obtained from [34, 35]:

$$r_{sh} = \frac{V_{oc}}{J_{sc}} \quad (10)$$

Together, these parameters not only quantify the overall efficiency of the device but also provide deeper physical insight into the underlying loss mechanisms. The ability to link absorption enhancement from plasmonic NPs

ARTICLE IN PRESS

with improvements in J_{SC}, V_{OC}, FF, and ultimately PCE is central to evaluating the true potential of the proposed nanostructured CIGS solar cells.

3. Results and Discussion

The performance analysis began with the evaluation of the reference non-plasmonic CIGS solar cell. As summarized in Table 2, this bare configuration achieved a short-circuit current density (Jsc) of 22.50 mA/cm² and a power conversion efficiency (PCE) of 12.97%, serving as the baseline for comparison. In this work, full cylindrical nanoparticles are initially considered as a conventional plasmonic reference geometry to establish a baseline for comparison with modified designs. The single semi-cylindrical nanoparticle (SNP) is then introduced as an optimized geometry, where half of the metallic volume is removed to reduce parasitic absorption and to enhance electromagnetic field penetration into the CIGS absorber through the flat metal–semiconductor interface. After demonstrating that SNPs consistently outperform full cylinders in terms of useful absorption and J_{SC}, subsequent analyses focus on SNP and DNP configurations, while the full cylinder geometry is excluded to avoid redundancy and to highlight the physical advantages of the optimized designs. For a comprehensive assessment, five metallic materials, Ag, Au, Al, Ni, and Ti, were investigated. As shown in Figure 2a, spherical NPs with radii ranging from 10 to 100 nm were analyzed, followed by cylindrical nanoparticles of the same range and a fixed height of 120 nm (Figure 2b). In both geometries, the J_{SC} initially increased with NP radius, reaching an optimal size before declining due to parasitic absorption within the metal.

In Figures 2(c) and 2(d), nanoparticle radii were limited to $R \leq 55$ nm due to the observation that beyond this value, the benefits of increased radius were outweighed by increased parasitic absorption within the metal. Larger nanoparticles also led to more complex interactions and reduced the overall plasmonic coupling efficiency, which in turn diminished the net optical enhancement. Thus, R = 55 nm was identified as the optimal radius for achieving the highest light absorption and short-circuit current density (J_{SC}) without compromising efficiency. Also, in Figure 2, the interparticle spacing, d, is set to 40 nm for the sphere and cylinder configurations, and for the double hemi-cylindrical (DNP) configuration.

To provide a clear quantitative comparison of the photovoltaic enhancement achieved by different NPs geometries and materials, Figure 3 summarizes the J_{SC} values for all investigated cases, along with the reference bare cell (indicated by the dashed line). As evident from the bar chart, the integration of plasmonic nanoparticles significantly improves the current density compared to the non-plasmonic structure. Among the simulated materials, Ag and Au demonstrate the highest J_{SC} values across all geometries, confirming their superior plasmonic response. Furthermore, the dual semi-cylinder (DNP) configuration consistently achieves the greatest enhancement for each metal, clearly outperforming the single semi-cylinder (SNP), sphere, and

ARTICLE IN PRESS

cylinder designs. For Ag, J_{SC} rises from 29.88 (mA/cm²) (SNP) to 31.12 (mA/cm²) (DNP), evidencing the constructive

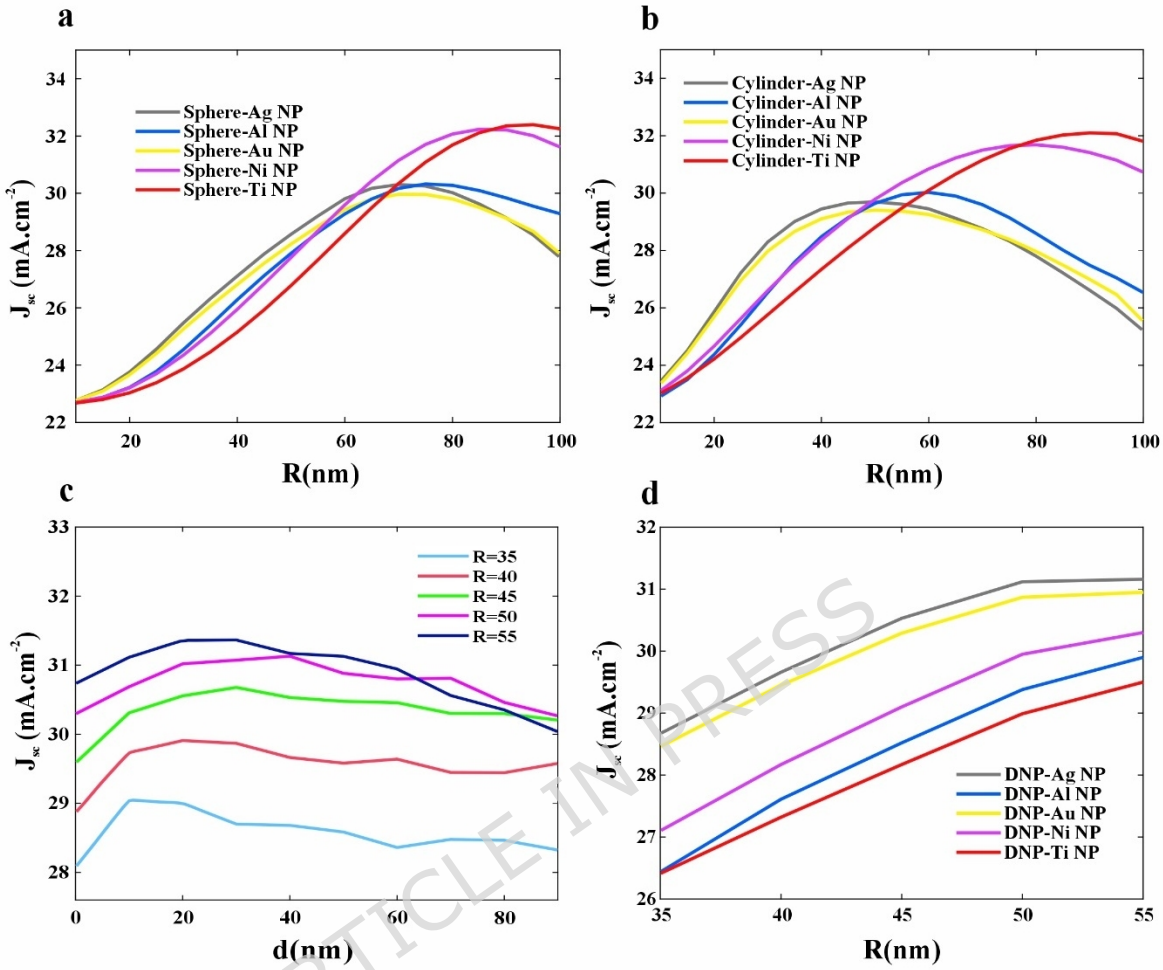

Figure 2. Short-circuit current density (Jsc) as a function of nanoparticle radius and spacing: (a) spherical NPs of different materials (Ag, Au, Al, Ni, Ti); (b) cylindrical NPs; (c) variation of Jsc with radius (R) and inter-particle gap (d) for Ag DNP; and (d) Jsc as a function of radius (R) for DNPs composed of different metals (Ag, Au, Al, Ni, Ti).

plasmonic coupling effect between the paired NPs. This overall comparison underscores that the DNP geometry provides the most effective light–matter interaction and photocurrent generation among all examined configurations, establishing it as the optimal design for subsequent analyses.

In Figure 3, the semi-circular configuration (SNP and DNP) outperforms the spherical and cylindrical geometries for Ag and Au due to their stronger plasmonic responses at the resonance wavelengths. The semi-circular shape allows for more effective plasmonic coupling, enhancing near-field light trapping and resulting in a higher short-circuit current density (J_{SC}). In contrast, for metals such as Al, Ni, and Ti, which exhibit weaker plasmonic resonances, the semi-circular geometry does not enhance absorption as effectively and can even lead to increased parasitic losses, thereby degrading

ARTICLE IN PRESS

device performance. In these metals, spherical and cylindrical configurations are more effective in optimizing light absorption.

For clarity, the J_{SC} values reported in Figure 3 were extracted at the optimized dimensions of each geometry. For spherical and full cylindrical nanoparticles, R was taken at the maximum of the corresponding $J_{SC}(R)$ curves in Figure 2(a) and Figure 2(b) for each metal (with h=120 nm for cylinders). For the semi-cylindrical designs, the optimized geometry was used, and for DNPs the parameters R=50 nm and d=40 nm (Table 1) were applied (with h=120 nm). Thus, Figure 3 represents a best-case comparison between geometries rather than a single fixed (R, d) condition.

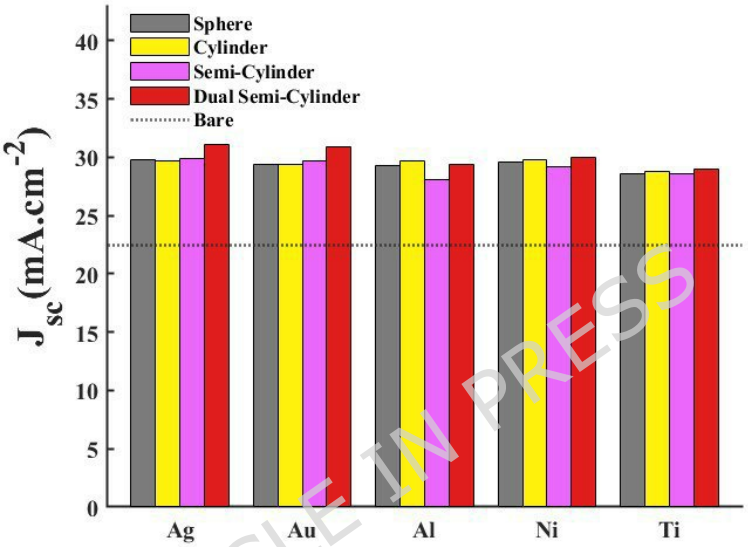

Figure 3. Comparison of J_{SC} values for sphere NPs, cylinder NPs, semi-cylinder NPs and dual semi-cylinder NPs structures for different materials.

The significant improvement in J_{SC} observed across the various plasmonic geometries strongly suggests that localized surface plasmon resonances (LSPRs) play a dominant role in enhancing optical absorption within the CIGS layer. To gain deeper insight into this phenomenon and to directly link the electrical improvements to the optical origin, it is crucial to analyze the absorption spectra of the proposed structures. The following section, therefore, focuses on the wavelength-dependent absorption characteristics, enabling a clearer understanding of how nanoparticle geometry and material composition influence light trapping, field confinement, and overall absorption enhancement in the ultrathin solar cell. Figure 4 illustrates the influence of NPs geometry and material composition on the optical absorption and parasitic losses of ultrathin CIGS solar cells. Figures 4a and b compare spherical and cylindrical NPs made of Ag, Au, Al, Ni, and Ti metallic NPs. As seen in the Figures. 4a and b, all types of NPs enhance the overall absorption within the active CIGS layer across the visible and near-infrared spectrum (300–900 nm) compared to the bare structure. Among the spherical geometries, Ag and Au NPs show the strongest plasmonic response,

ARTICLE IN PRESS

producing distinct resonance peaks near 800 nm. This enhancement originates from LSPR, which concentrates electromagnetic fields near the metal–semiconductor interface and effectively increases the optical path length within the absorber. Al NPs, with its higher plasma frequency, contributes to a broader but weaker enhancement in the shorter wavelengths (400–600 nm), while Ni and Ti exhibit lower optical intensities due to higher intrinsic damping. On the other hand, the cylindrical NPs maintain a similar spectral behavior but with a slight red-shift of the resonance peak, attributed to their elongated geometry and increased aspect ratio, as shown in Figure 4b. This shift results in improved light trapping in the near-infrared region where the CIGS absorption coefficient is lower, thereby extending the absorption bandwidth.

While plasmonic NPs significantly enhance light absorption within the CIGS layer, a portion of the incident energy is inevitably dissipated as parasitic losses within the metallic nanostructures. These losses, illustrated in the corresponding absorption loss spectra of Figures 4c and d, originate primarily from Joule heating associated with the imaginary part of the dielectric function of metals. Understanding this trade-off between useful absorption and optical dissipation is essential for achieving optimal device performance. Figures 4c and 4d display the corresponding parasitic absorption losses in the metallic NPs. It is evident that Ti and Ni exhibit the highest losses, particularly in the longer wavelength region, owing to their higher imaginary permittivity. In contrast, Ag and Al NPs demonstrate significantly lower parasitic absorption, confirming their superior optical performance for plasmonic enhancement. To further enhance the light-trapping performance, plasmonic design was evolved from single NPs to coupled configurations.

ARTICLE IN PRESS

ARTICLE IN PRESS

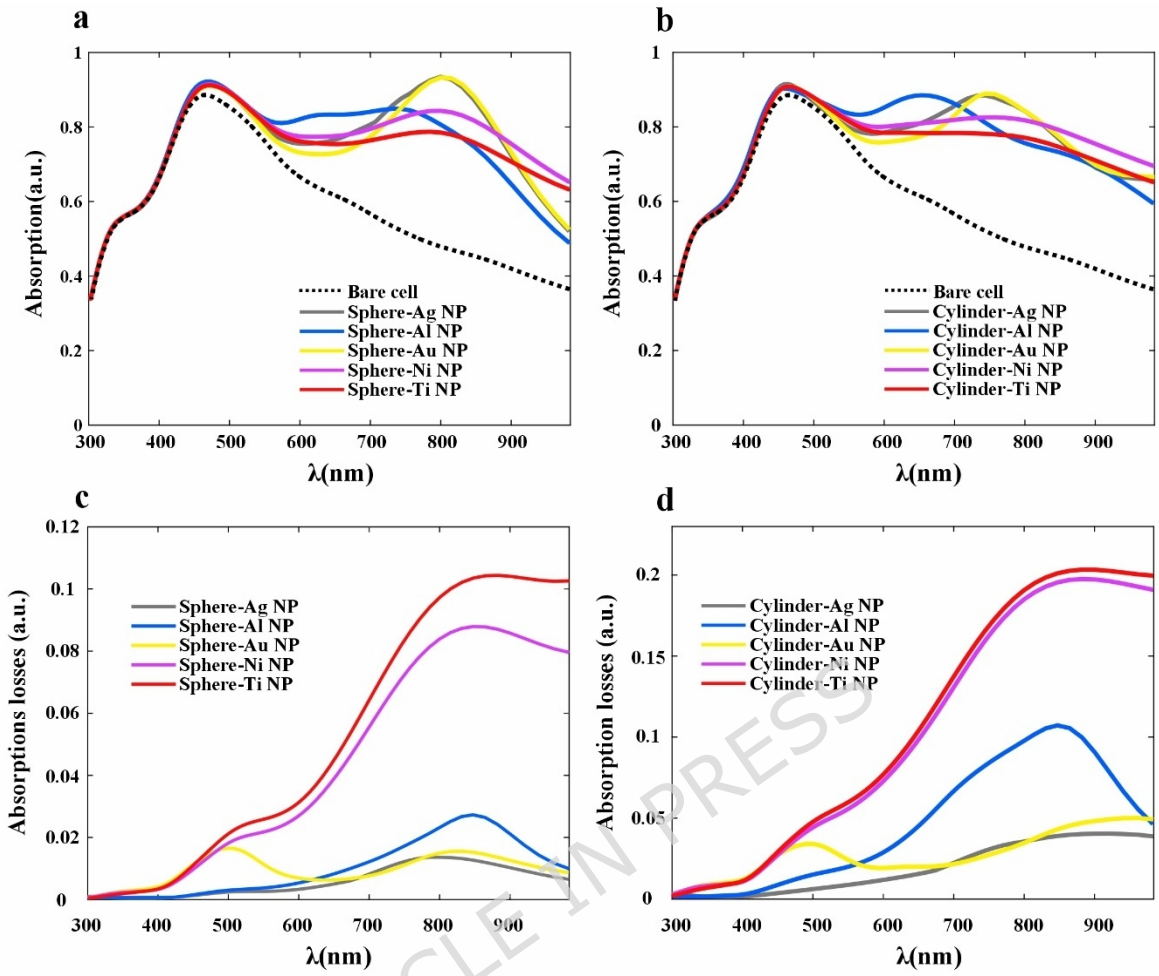

Figure 4. Absorption spectra of ultrathin CIGS solar cells with plasmonic NPs of different geometries: (a) spherical and (b) cylindrical for various metallic materials (Ag, Au, Al, Ni, and Ti); corresponding absorption loss spectra are shown in (c) and (d), respectively.

Figure 5 compares the optical absorption and corresponding losses for single semi-cylindrical (SNP) and double semi-cylindrical (DNP) NPs embedded at the center of the CIGS absorber. As shown in the Figures. 5a and 5b, the design of the SNP significantly improves absorption compared to the spherical and cylindrical cases, owing to better field confinement along the flat-curved interface. More importantly, when two half-cylinders are placed adjacent to each other (DNP configuration), a pronounced enhancement is observed across the visible–NIR region. This is attributed to the plasmonic coupling between neighboring NPs, which induces hybridized modes that strengthen both the near-field intensity and far-field scattering efficiency. The coupling effect effectively broadens the resonance spectrum and increases light confinement within the 200 nm absorber. Figures 5c and 5d present the corresponding absorption losses in the metal regions. Although DNP structures introduce slightly higher local absorption within the metal, the gain in useful absorption within the CIGS layer far outweighs this penalty.

ARTICLE IN PRESS

Among all materials, Ag-based DNPs exhibit the optimal balance between high plasmonic enhancement and minimal parasitic loss. A quantitative summary of the photovoltaic performance parameters is presented in Table 2.

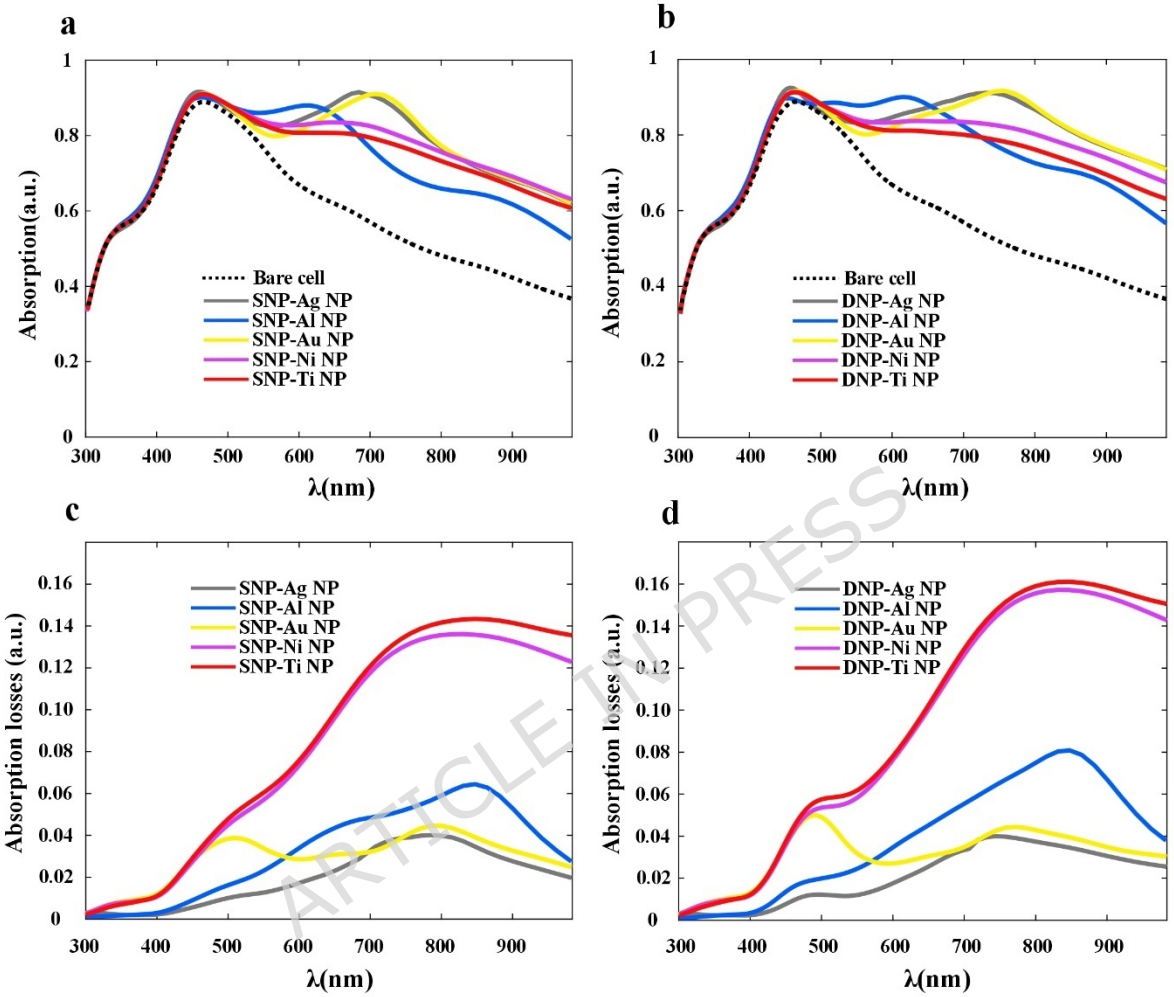

Figure 5. Absorption spectra of ultrathin CIGS solar cells incorporating plasmonic nanoparticles with semi-cylindrical geometries: (a) single (SNP) and (b) double (DNP); corresponding absorption loss spectra for (c) SNP and (d) DNP configurations.

To further quantify the broadband optical enhancement, the spectral absorption rate (SAR) was calculated by integrating the absorption spectrum weighted with the standard AM1.5G solar irradiance over the entire wavelength range. The SAR values, together with the percentage improvements in SAR (ΔSAR) and power conversion efficiency (ΔPCE) relative to the bare device, are summarized in Table 2. The results show that all plasmonic configurations improve broadband absorption compared to the bare CIGS cell. Among them, the DNP configuration exhibits the highest enhancement, indicating that plasmonic coupling effectively increases light

ARTICLE IN PRESS

trapping and contributes to the observed improvement in photovoltaic performance.

Table 2. Summary of the simulated photovoltaic characteristics for ultrathin CIGS solar cells with different plasmonic configurations.

Material	Geometry	Jsc (mA/cm²)	Voc (V)	FF (%)	PCE (%)	ΔPCE (%)	SAR	ΔSAR (%)
Bare Cell	—	22.50	0.685	84.15	12.97	-	0.639	-
Ag	Sphere	29.81	0.692	84.20	17.34	33.69	0.801	25.35
Ag	Cylinder	29.69	0.692	84.20	17.27	33.15	0.800	25.20
Ag	SNP	29.88	0.693	84.27	17.44	34.46	0.810	26.76
Ag	DNP	31.12	0.694	84.29	18.20	40.32	0.847	32.55
Au	Sphere	29.42	0.692	84.10	17.10	31.84	0.791	23.79
Au	Cylinder	29.40	0.692	84.10	17.09	31.77	0.793	24.10
Au	SNP	29.72	0.693	84.18	17.30	33.38	0.804	25.82
Au	DNP	30.87	0.694	84.28	18.04	39.09	0.829	29.73
Al	Sphere	29.27	0.691	84.05	17.00	31.07	0.796	24.57
Al	Cylinder	29.64	0.692	84.15	17.22	32.77	0.804	25.82
Al	SNP	28.04	0.689	84.00	16.20	24.90	0.771	20.66
Al	DNP	29.38	0.692	84.26	17.14	32.15	0.801	25.35
Ni	Sphere	29.59	0.692	84.10	17.25	32.92	0.797	24.73
Ni	Cylinder	29.78	0.692	84.20	17.37	33.93	0.802	25.51
Ni	SNP	29.22	0.691	84.05	17.05	31.46	0.793	24.10
Ni	DNP	29.95	0.693	84.27	17.48	34.77	0.809	26.60
Ti	Sphere	28.59	0.690	84.00	16.58	27.83	0.775	21.28
Ti	Cylinder	28.80	0.691	84.05	16.72	28.92	0.780	22.07
Ti	SNP	28.54	0.690	84.00	16.55	27.60	0.777	21.60
Ti	DNP	28.99	0.691	84.26	16.90	30.30	0.787	23.16

ARTICLE IN PRESS

The absorption spectra clearly reveal that the dual semi-cylindrical design yields the strongest broadband enhancement, particularly for Ag-based structures. However, understanding why this geometry outperforms the others requires examining how electromagnetic energy is distributed and confined within the device. To elucidate the physical mechanism underlying the observed absorption improvement, the spatial distribution of the electric field intensity was analyzed for both single (SNP) and dual (DNP) configurations at representative resonance wavelengths. The electric-field intensity distributions shown in Figure 6 are calculated for the optimized Ag semi-cylindrical nanoparticle geometries. In all cases, the nanoparticle radius is fixed at R = 50 nm, while the inter-particle gap in the DNP configuration is d = 40 nm, corresponding to the optimal parameters that yield the maximum J_{SC}. The electric-field intensity maps in Figure 6 compare the near-field distributions of a single Ag semi-cylinder (top row, Figures a–c) and the double half-cylinder (bottom row, Figures d–f) at three representative wavelengths (λ = 457nm, 615 nm, and 731 nm). These snapshots reveal three physical trends: (i) the modal character of the resonances evolves with

ARTICLE IN PRESS

wavelength, (ii) plasmonic coupling in the DNP geometry redistributes and amplifies the near field (especially in the gap), and (iii) the enhanced near fields in the DNP translate into stronger local generation in the thin (200 nm) CIGS absorber.

At the shortest wavelength (λ = 457 nm, Figures 6a and 6d), the SNP exhibits moderate edge hot spots located at the flat–curved junctions; the field pattern is characteristic of a higher-order or off-resonant excitation where surface curvature concentrates fields at sharp features. In the DNP case, similar hot spots appear around each semi-cylinder, but now symmetry and the proximity of the partners produce additional field reinforcement at the outer edges and along the faces facing away from the gap (see Figure 6d). Although the spectral response at this wavelength is not the strongest resonance of the system, the DNP geometry already shows a more spatially widespread near-field distribution, which increases the interaction volume inside the absorber.

At the intermediate wavelength (λ = 615 nm, Figures 6b and 6e), the maps show a stronger and more clearly defined rim of high intensity along the curved surface of the SNP. As illustrated in Figure 6b, for the SNP, the intensity is concentrated along the curved rim and near the flat face; this is consistent with the dominant dipolar-like plasmon mode that enhances fields close to the metal–semiconductor interface. In the DNP, the two rims are brighter and show a periodic structure around the curved edges a clear signature of near-field hybridization (see figure 6e). The presence of the neighbor splits and broadens the modal response energy that, in the single particle, resides only on one rim, is redistributed into coupled modes that occupy both particles and the region between them, increasing the integrated field in the absorber.

ARTICLE IN PRESS

ARTICLE IN PRESS

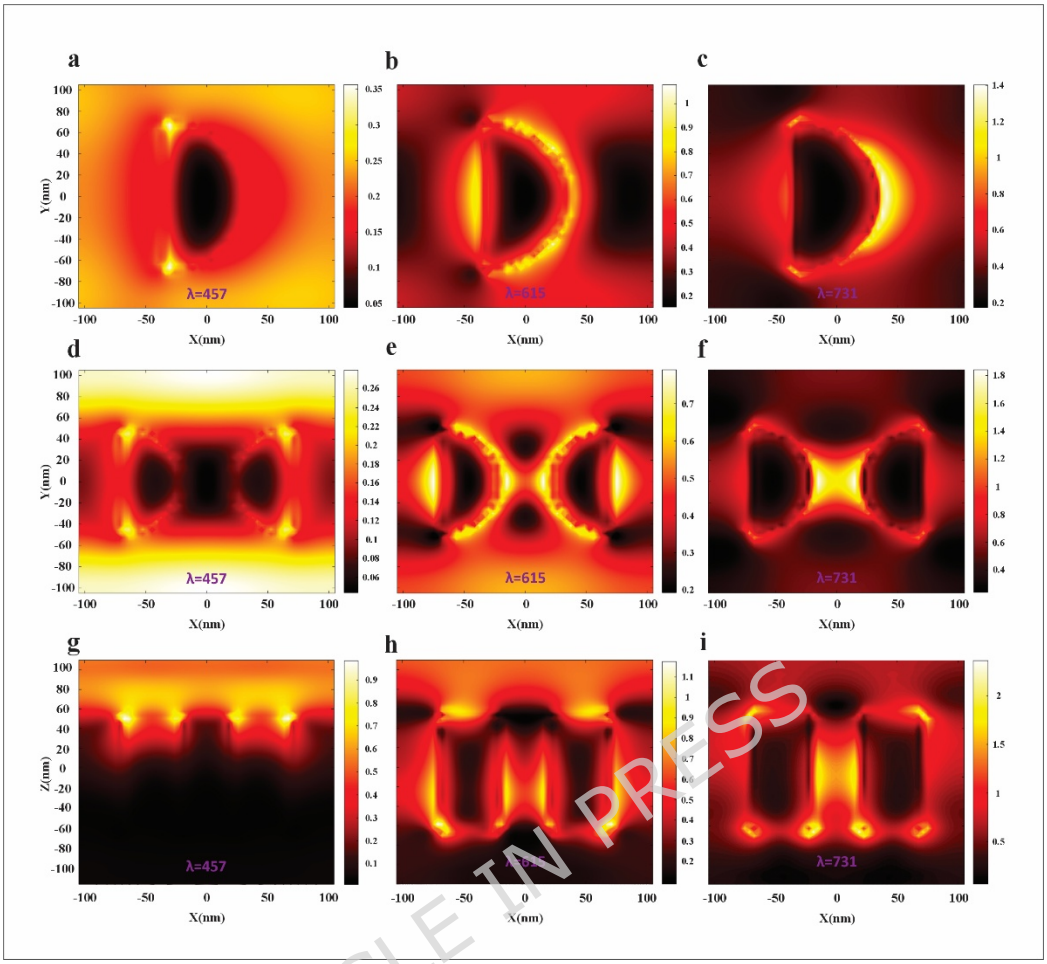

Figure 6. Comparison of the electric field intensity enhancement ($|E|^2/|E_0|^2$) profiles for the optimized (a–c) Ag SNP, and (d–f) Ag DNP structures and (g-i) Ag DNP structures in a cross-sectional view at 457 nm, 615 nm, and 731 nm wavelengths.

ARTICLE IN PRESS

At the longest wavelength (λ = 731 nm, Figures 6c and 6f) the difference is most striking. As Figure 6c shows, the SNP supports a strong localized field mainly on the exposed curved side the expected single-particle resonance near the longer-wavelength LSPR. In contrast, the DNP displays an intense, centrally concentrated hot spot at the narrow region between the two halves (the gap) in addition to strong rim fields. This central hot spot is a direct manifestation of plasmonic mode hybridization (bonding-like coupled mode) and produces the largest local field enhancements. Quantitatively, the coupled configuration increases the near-field intensity at the resonance by a substantial fraction (the optimized DNP reported a ≈29% larger near-field metric at λ ≈ 731 nm compared with the SNP), explaining the observed increase in optical generation and J_{SC} for the DNP geometry.

In other words, Figure 6 shows the trade-off and the benefit of coupling. DNPs produce larger local fields and, therefore, a higher local generation rate precisely in regions spatially collocated with the active semiconductor, thereby increasing useful absorption. At the same time, the strong

ARTICLE IN PRESS

localization at metal surfaces implies greater parasitic absorption in the metal; however, for Ag DNPs, the net balance favors the semiconductor because silver's relatively low loss and high scattering cross-section channel more energy into the absorber than into Joule heating. The evolution from edge-localized hot spots for SNPs at short wavelengths, to a dominant gap hot spot DNP at resonance wavelength is the essential mechanism by which the DNP architecture extends the effective optical path length inside a 200 nm absorber and raises J_{SC}.

The spatial distribution of the optical generation rate provides valuable insight into how effectively absorbed photons contribute to charge carrier generation within the CIGS absorber. As shown in Figure 7, the regions surrounding the plasmonic NPs exhibit a pronounced enhancement in optical generation rate, particularly near the metal–semiconductor interfaces where LSPRs strongly amplify the near-field intensity.

The generation-rate maps compare the spatial distribution of photo-generated carriers for Ag and Au half-cylindrical NPs in SNP and DNP arrangements. Figures 7a and 7c correspond to Au (SNP and DNP), Figures 7b and 7d to Ag (SNP and DNP). Two observations are clear: (i) Ag produces systematically larger and more extended generation hotspots than Au for the same geometry, and (ii) the DNP arrangement enhances and concentrates generation in the gap region for both metals, but the effect is stronger and more spatially extensive for Ag. From a physical standpoint, the difference between Ag and Au originates from their distinct dielectric behaviors in the visible–near-infrared region. Au experiences stronger interband damping at shorter visible wavelengths, which diminishes the near-field intensity and weakens the effective LSPR compared to Ag.

The result is that, for equivalent geometry and excitation, Au yields lower local ($|E|^2$) and thus a lower local generation rate. This explanation is consistent with the observed lower amplitudes in Figures 7a and 7c relative to 7b and 7d. Looking at geometry, the SNP maps already show rim-localized generation near the metal–semiconductor interface.

ARTICLE IN PRESS

ARTICLE IN PRESS

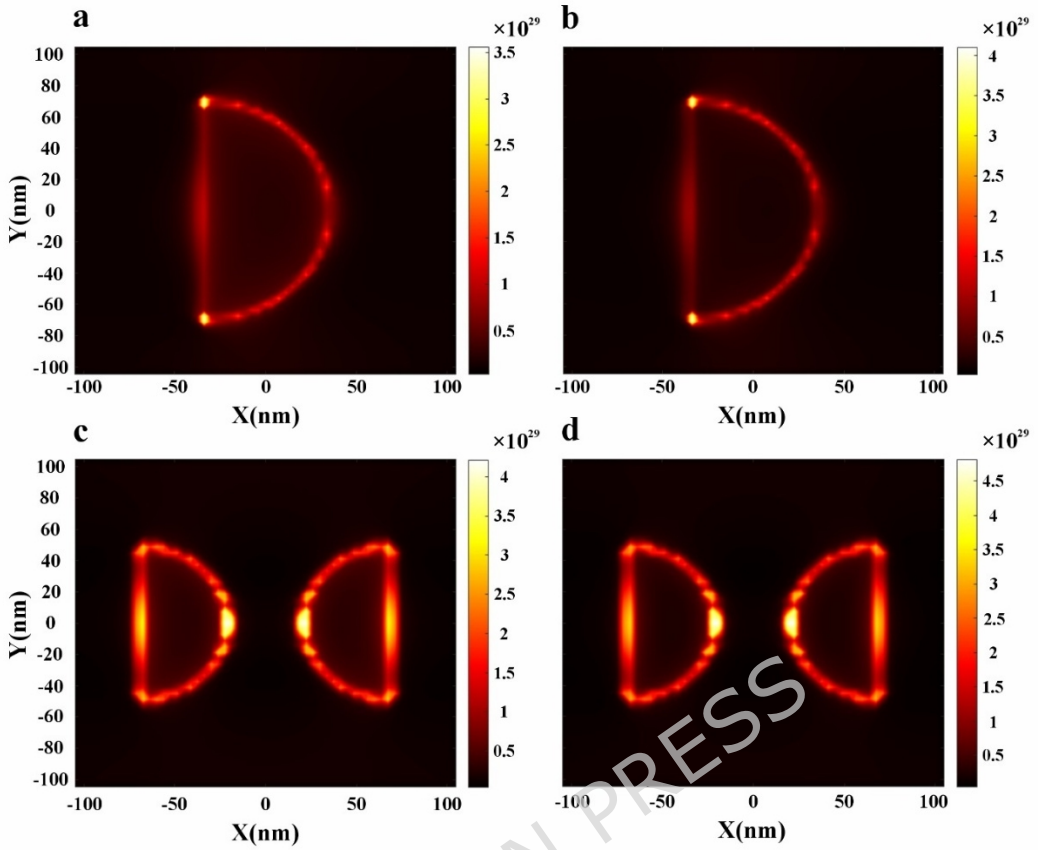

Figure 7. (a,c) Optical generation rate profiles ($cm^{-3}.s^{-1}$) for Au-based SNP and DNP structures and (b,d) for Ag-based structures.

Under practical conditions, the numerical difference remains modest, with Ag exhibiting slightly superior performance to Au in the optimized geometries; however, this improvement is consistent and physically meaningful. Two physical scenarios can ensue. First, when the objective is purely maximizing near-term optical generation in ultrathin absorbers, Ag especially in the coupled DNP structure is preferable because of its higher scattering efficiency and lower damping in the visible. Second, if long-term chemical inertness under operation were the dominant constraint, Au could be considered despite its lower optical generation rate here; however, the combination of Ag's superior optical performance and the demonstrated tolerance to thin native oxide (Ag_2O) in our oxidation tests makes Ag a more cost-effective and high-performance choice for scalable CIGS devices.

Figure 8 illustrates the influence of surface 3nm oxidation on the optical absorption characteristics of ultrathin CIGS solar cells integrated with different plasmonic NPs Ag, Al, Ni, and Ti. Each Figure compares the absorption spectra of the bare cell (black dashed line) with those obtained before and after oxidation of the metallic NPs. In Figure 8a, the Ag NPs exhibit the strongest plasmonic resonance among all studied materials, showing a pronounced absorption peak in the 450–550 nm range due to LSPR. After oxidation, corresponding to the formation of a thin Ag_2O shell,

ARTICLE IN PRESS

the intensity of the resonance slightly decreases but remains significantly higher than that of the bare cell. This moderate decline indicates that the Ag_2O shell only marginally attenuates the plasmonic coupling while contributing to long-term surface stability. Therefore, Ag-based nanoparticles represent the most efficient and practical choice for optimizing optical absorption in ultrathin CIGS devices.

The observed enhancement trends are consistent with previously reported experimental studies on plasmonic thin-film solar cells, where metallic nanoparticles improve device performance through near-field enhancement and scattering-induced light trapping [36, 37]. In particular, experimental reports indicate that coupled nanoparticle configurations lead to stronger field localization and broader spectral absorption compared to isolated nanoparticles, which agrees well with the trends predicted by the present simulations. In Figure 8b, Al NPs enhance light absorption primarily in the ultraviolet and visible regions. Following oxidation (formation of Al_2O_3), a small drop in absorption is observed, yet the overall response remains stable. The presence of the Al_2O_3 shell can serve as a natural passivation layer, protecting the nanoparticles and maintaining good optical performance. Figures 8c and 8d present the behavior of Ni NPs and Ti NPs, respectively. Both materials exhibit more moderate absorption enhancement compared to Ag and Al. The oxidation of Ni to NiO and Ti to TiO_2 results in a slight suppression of the plasmonic resonance, which can be attributed to the increased damping and reduced conductivity of the oxide shells. However, the spectral profiles remain smooth and stable, suggesting their potential use in robust or thermally demanding environments.

ARTICLE IN PRESS

ARTICLE IN PRESS

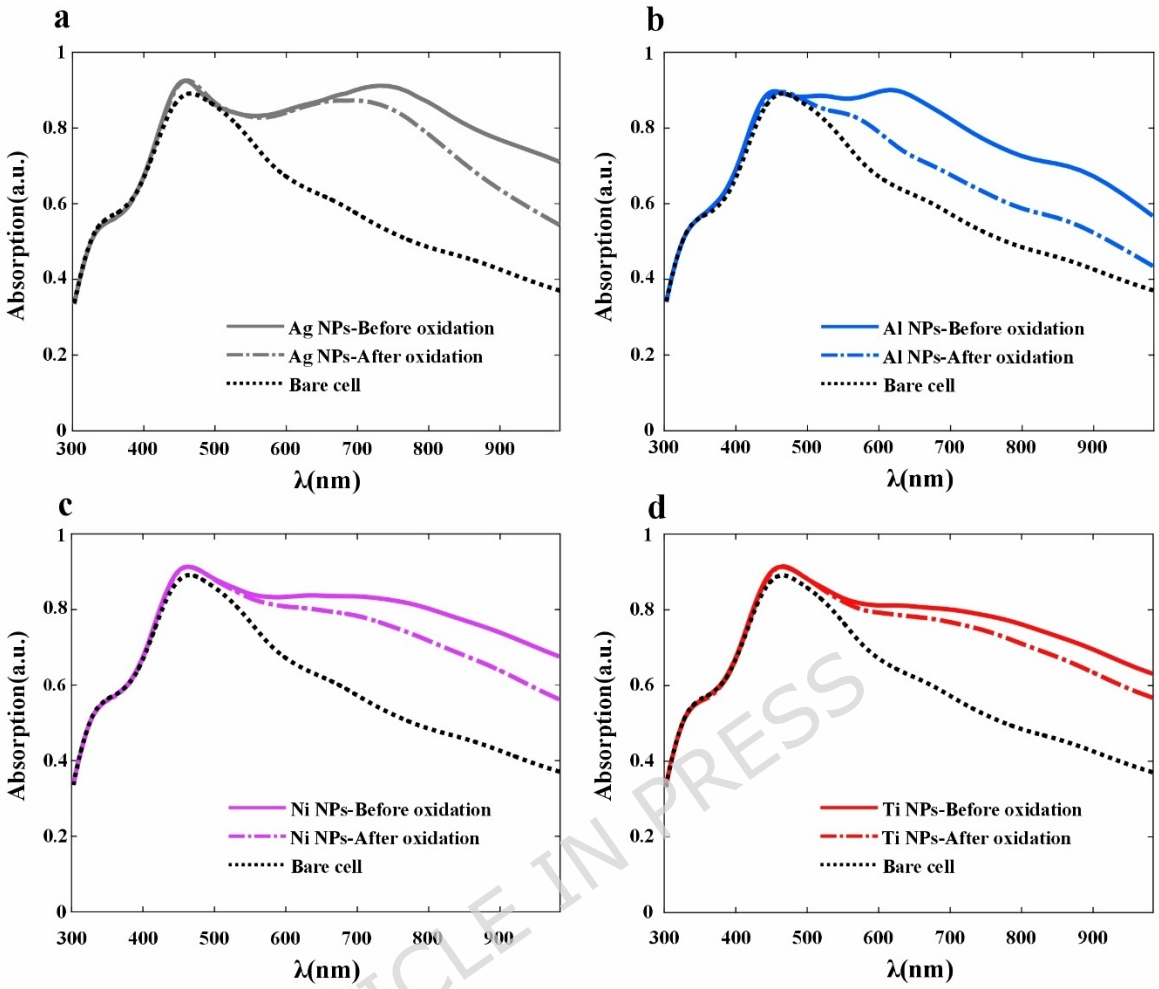

Figure 8. Effect of a 3 nm oxide shell a) Ag_2O, b) Al_2O_3, c) NiO, and d) TiO_2 on the absorption of DNP structures

It should be noted that Au was not considered in this oxidation analysis, as its superior chemical stability makes surface oxidation effects negligible compared to the other metals. Overall, the results confirm that Ag-based NPs offer the optimal plasmonic performance, achieving the highest absorption enhancement even after oxidation, while maintaining a favorable trade-off between optical gain and structural durability. This demonstrates the practicality of using Ag with a controlled oxide shell for stable, high-efficiency ultrathin CIGS photovoltaic applications.

To better visualize the numerical trends reported in Table 3, the variations in J_{SC} before and after oxidation are depicted in Figure 9 for all investigated DNP materials.

Figure 9 illustrates the variation in J_{SC} for the DNP structures before and after oxidation across different metallic materials. The yellow bars correspond to pristine NPs, while the orange bars represent the oxidized cases with a 3 nm oxide shell. As shown, oxidation slightly reduces J_{SC} in all

ARTICLE IN PRESS

cases due to increased damping and weakened plasmonic coupling. The reduction magnitude varies among the materials, with approximately 13% for Al, 6% for Ni, 5% for Ag, and 4% for Ti. Despite this decrease, all oxidized DNP structures still outperform the bare cell J_{SC} of 22.50 (mA/cm²), demonstrating that the plasmonic enhancement remains robust under oxidation. Among them, Ag–DNP maintains the highest Jsc of 29.44 (mA/cm²), confirming its optimal trade-off between plasmonic efficiency and long-term environmental stability.

Table 3. Effect of surface oxidation on J_{SC} for various plasmonic DNP structures.

Material	J_{SC} (mA/cm²) before oxidation	J_{SC} (mA/cm²) after oxidation
Ag	31.12	29.44
Al	29.38	25.57
Ni	29.95	28.14
Ti	28.99	27.86

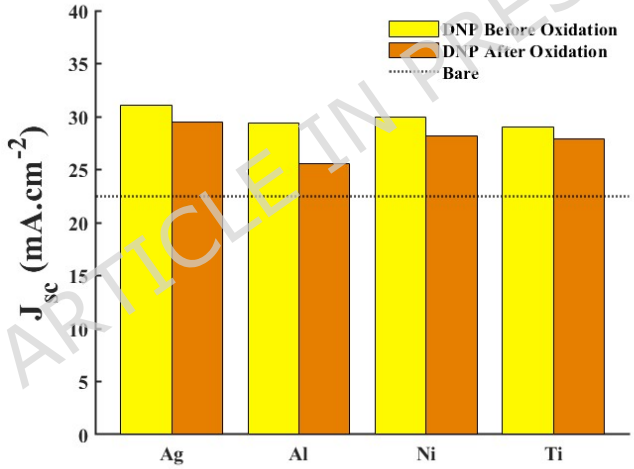

Figure 9. Comparison of J_{SC} before and after oxidation for different DNP-based plasmonic structures.

Figure 10 presents a comparative analysis between the single- and dual-nanoparticle designs for the optimized Ag structures. As shown in Figure 10a, the DNP configuration demonstrates a noticeably stronger and broader enhancement compared with the SNP, particularly at wavelengths longer than 710 nm, where the near-field coupling between adjacent semi-cylindrical nanoparticles significantly amplifies the local electromagnetic intensity. This enhanced coupling results in improved photon confinement

ARTICLE IN PRESS

and increased carrier generation within the 200 nm CIGS absorber, and this optical improvement translates directly into superior electrical performance. The electrical response of these structures, shown in Figure 10b, confirms this optical improvement. The J–V characteristics reveal that both SNP and DNP designs markedly outperform the non-plasmonic reference cell. Among them, the Ag DNP achieves the highest J_{SC} of 31.12 (mA/cm²), along with a slightly higher open-circuit voltage and fill factor, leading to a substantial improvement in power conversion efficiency (PCE). This performance gain directly reflects the constructive plasmonic coupling effect and the efficient redistribution of the electromagnetic field inside the absorber region. To benchmark the obtained results against the state of the art, Table 4 provides a comparative summary between this work and previously reported plasmon-enhanced CIGS and thin-film photovoltaic devices. The results clearly demonstrate that the optimized Ag DNP design not only achieves one of the highest reported J_{SC} and PCE values among similar studies but also maintains a favorable trade-off between optical enhancement, electrical performance, and structural simplicity. Underscoring its potential for practical integration into next-generation ultrathin solar cells.

ARTICLE IN PRESS

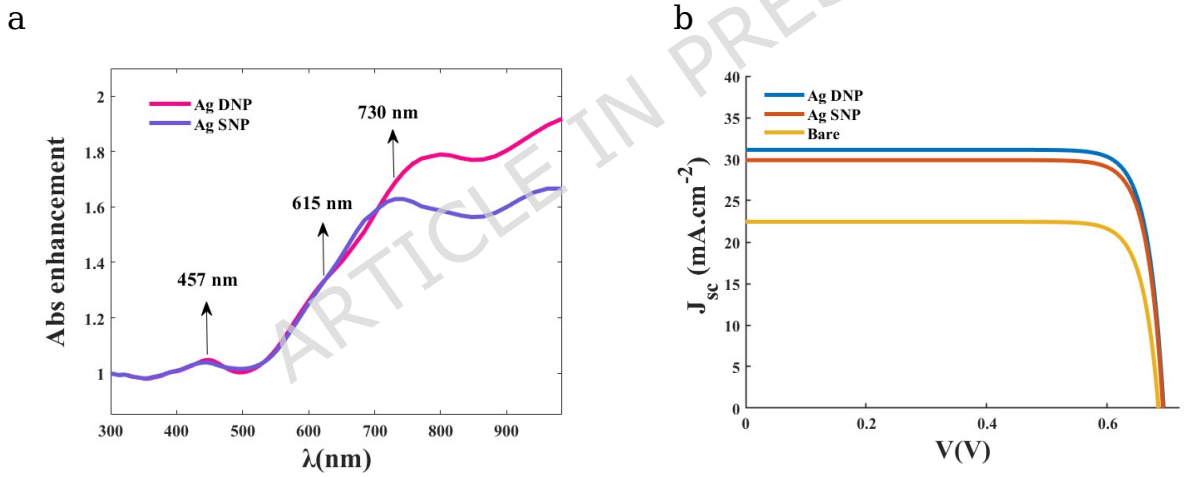

Figure 10. Comparison of optical and electrical performance for optimized Ag-based structures: (a) Absorption enhancement spectra of SNP and DNP configurations, (b) J–V characteristics of the corresponding devices.

Table 4. Comparison of the simulated results of this work with previously similar studies.

Reference	Main Research Approach	Thickness	Jsc (mA/cm²)
Present Study	Ultra-Thin with Plasmonic Optimization	200 (nm)	31.12
Study [38]	Ultra-Thin (Baseline without EBR)	500 (nm)	30.60
Study [39]	Thickness Reduction Study	400 (nm)	28.97
Study [40]	Analytical Modeling	1000 (nm)	32.75
Study [41]	Thickness Reduction Study	1000 (nm)	36.45
Study [42]	Structure Optimization (light management)	2000 (nm)	36.5

ARTICLE IN PRESS

Conclusion:

In this study, a comprehensive optical and electrical analysis of an ultrathin CIGS solar cell integrated with plasmonic nanoparticles was performed using the 3D FDTD method. The investigation aimed to enhance light absorption and carrier generation in the 200 nm absorber layer without increasing material consumption. Various nanoparticle geometries, spherical, cylindrical, single semi-cylindrical (SNP), and double semi-cylindrical (DNP), and multiple metallic compositions (Ag, Au, Al, Ni, Ti) were systematically examined. The results revealed that the DNP configuration provides the most effective light–matter interaction due to the strong plasmonic coupling between adjacent particles, which broadens the resonance bandwidth and intensifies the local electromagnetic field. Among the investigated materials, silver (Ag) demonstrated the best overall performance, yielding a J_{SC} of 31.12 (mA/cm^{-2}) and a PCE of 18.20%, representing a remarkable improvement over the non-plasmonic reference cell (Jsc = 22.50 (mA/cm^{-2}), PCE = 12.97%). The enhanced performance originates from more efficient light scattering, extended optical path length, and intensified near-field confinement around the nanoparticles.

To ensure the practicality and stability of the design, the impact of surface oxidation on different plasmonic materials was also evaluated. The results confirmed that, although oxidation slightly decreases the photocurrent, Ag-based DNPs maintain a superior balance between optical gain and environmental durability, retaining a high Jsc of 29.44 (mA/cm^{-2}) after oxidation. Although Au-based DNPs exhibit a slightly higher J_{SC} in the pristine state, Ag is selected as the optimal plasmonic material because it provides the highest intrinsic photocurrent enhancement before oxidation and retains strong performance after oxidation, with only a minor reduction in J_{SC}. Moreover, Ag offers lower parasitic optical losses, stronger scattering efficiency in the visible–NIR region, and significantly lower material cost compared to Au. These combined optical and practical advantages make Ag-based DNPs the most suitable choice for scalable ultrathin CIGS solar cells. These findings underline the potential of Ag DNPs as a viable route for achieving efficient and stable ultrathin CIGS photovoltaic devices.

Declarations

Data Availability

The data that support the findings of this study are available from the corresponding author upon reasonable request.

Competing Interests

The authors declare no competing interests.

Funding

No funding was received for conducting this research.

ARTICLE IN PRESS

Reference:

1. Mufti, N., et al., Review of CIGS-based solar cells manufacturing by structural engineering. Solar energy, 2020. 207: p. 1146-1157.
2. Jangjoy, A., H. Bahador, and H. Heidarzadeh, Design of an ultra-thin silicon solar cell using localized surface plasmonic effects of embedded paired nanoparticles. Optics Communications, 2019. 450: p. 216-221.
3. Repins, I., et al., 19· 9%-efficient ZnO/CdS/CuInGaSe2 solar cell with 81· 2% fill factor. Progress in Photovoltaics: Research and applications, 2008. 16(3): p 235-239.
4. Sivasankar, S.M., C.d.O. Amorim, and A.F.d. Cunha, Progress in thin-film photovoltaics: A review of key strategies to enhance the efficiency of CIGS, CdTe, and CZTSSe solar cells. Journal of Composites Science, 2025. 9(3): p. 143.
5. Kovacic ,M., et al., Light management design in ultra-thin chalcopyrite photovoltaic devices by employing optical modelling. Solar Energy Materials and Solar Cells, 2019. 200: p. 109933.
6. Lopes, T.S., et al., Rear optical reflection and passivation using a nanopatterned metal/dielectric structure in thin-film solar cells. IEEE Journal of Photovoltaics, 2019. 9(5): p. 1421-1427.
7. Zarerasouli, P., H. Bahador, and H. Heidarzadeh, Performance improvement of an ultra-thin film solar cell based on optimized CIGS) Cu (In1-x, Gax) Se2) using appropriate plasmonic nanoparticles. Optical Materials, 2022. 131: p. 112729.
8. Day, J., S. Senthilarasu, and T.K. Mallick, Improving spectral modification for applications in solar cells: A review. Renewable Energy, 2019. 132 :p. 186-205.
9. Bahador, H., A. Jangjoy, and F. Aghaei, Synergistic Implementation of Nanophotonic and Plasmonic Structures for High-Efficiency Perovskite Solar Cells. Plasmonics, 2025: p. 1-13.
10. Jangjoy, A. and S. Matloub, Design of novel cubic nanoparticle for boosting performance of carbon-based perovskite solar cells. Solar Energy, 2025. 286: p. 113155.
11. Jangjoy, A., H. Bahador, and H. Heidarzadeh, A comparative study of a novel anti-reflective layer to improve the performance of a thin-film GaAs solar cell by embedding plasmonic nanoparticles. Plasmonics, 2021. 16(2): p. 395-401.
12. Jangjoy, A. and S. Matloub, Optimizing carbon-based perovskite solar cells with pyramidal core–shell nanoparticles for high efficiency. Plasmonics, 2025. 20(1): p. 265-275.
13. Khetri, M. and M.C. Gupta, Recycling of silver from CIGS solar cells using laser ablation and debonding. Solar Energy Materials and Solar Cells, 2025. 282: p. 113381.
14. Singh, G. and S. Verma, Design and analysis of thin film GaAs solar cells using silver nanoparticle plasmons. Photonics and Nanostructures-Fundamentals and Applications, 2019. 37: p. 100731.

ARTICLE IN PRESS

ARTICLE IN PRESS

15. Sharma, D., et al., Comparative numerical analysis of broadband light trapping structures based on plasmonic metals nanosphere and silicon nanopillar arrays for thin solar cells. Plasmonics, 2023. 18(2): p. 701-710.
16. Singh, G. and S. Verma, Plasmon enhanced light trapping in thin film GaAs solar cells by Al nanoparticle array. Physics Letters A, 2019. 383(13): p. 1526-1530.
17. Naik, G.V., V.M. Shalaev, and A. Boltasseva, Alternative plasmonic materials: alternative plasmonic materials: beyond gold and silver (adv. mater. 24/2013). Advanced Materials, 2013. 25(24): p. 3258-3258.
18. Jangjoy, A. and S. Matloub, Optical simulation and design of high-absorption thin-film perovskite halide solar cells based on embedded quadrilateral cluster nanoparticles. Solar Energy, 2022. 242: p. 10-19.
19. Bahador, H. and P. Zarerasouli, Novel Plasmonic Copper Nanostructures for High-Performance Ultra-Thin CIGS Solar Cells. Plasmonics, 2025: p. 1-10.
20. Akbari, M., F.D. Kashani, and S.M. Mirkazemi, Designing novel plasmonic architectures for highly efficient CIGS solar cells. Solar Energy, 2024. 274: p. 112589.
21. Movsesyan, A., et al., Hybridization and dehybridization of plasmonic modes. The Journal of Physical Chemistry C, 2020. 125(1): p. 724-731.
22. Huang, P., et al., Effect of selenization and sulfurization on the structure and performance of CIGS solar cell. Journal of Materials Science :Materials in Electronics, 2018. 29(2): p. 1444-1450.
23. Loubat, A., et al., Optical properties of ultrathin CIGS films studied by spectroscopic ellipsometry assisted by chemical engineering. Applied Surface Science, 2017. 421: p. 643-650.
24. Barreau ,N., et al., Innovative approaches in thin-film photovoltaic cells, in Optical Thin Films and Coatings. 2018, Elsevier. p. 595-632.
25. Mereu, R., et al., Optical and electrical studies of transparent conductive AZO and ITO sputtered thin films for CIGS photovoltaics. physica status solidi (c), 2014. 11(9-10): p. 1464-1467.
26. Singh, G. and S. Verma, Design and analysis of thin film GaAs solar cells using silver nanoparticle plasmons. Photonics Nanostruct Fundam Appl 37: 100731. 2019.
27. Palik, E.D., Handbook of optical constants of solids. Vol. 3. 1998: Academic press.
28. Zarerasouli, P., H. Bahador, and H.J.O.M. Heidarzadeh, Performance improvement of an ultra-thin film solar cell based on optimized CIGS (Cu (In1-x, Gax) Se2) using appropriate plasmonic nanoparticles. 2022. 131: p. 112729.
29. Lan, Y., et al., Fabrication of amorphous Al2O3 optical film with various refractive index and low surface roughness. 2020. 7(8): p. 086405.
30. Lamouri, A., et al., Morphological and spectroscopic ellipsometry investigations of NiO thin films fabricated by spray pyrolysis and spin-coating techniques: A comparative study. 2025.
31. Polyanskiy, M.N.J.S.D., Refractiveindex. info database of optical constants. 2024. 11(1): p. 94.

ARTICLE IN PRESS

ARTICLE IN PRESS

32. Sharma, D., et al., Comparative numerical analysis of broadband light trapping structures based on plasmonic metals nanosphere and silicon nanopillar arrays for thin solar cells. 2023. 18(2): p. 701-710.
33. Singh, G., J.S. Sekhon, and S. Verma, Plasmonic effects of Al nanoparticles embedded and non-embedded in thin film GaAs solar cells with Ta2O5 antireflective coating. Plasmonics, 2021. 16(6): p. 2091-2099.
34. Sarker, S., H.W. Seo, and D.M.J.J.o.P.S. Kim, Calculating current density–voltage curves of dye-sensitized solar cells: a straight-forward approach. 2014. 248: p. 739-744.
35. Williams, B.L., et al., Identifying parasitic current pathways in CIGS solar cells by modelling dark J–V response. 2015. 23(11): p. 1516-1525.
36. Subhan, A. and A.-H.I. Mourad, Plasmonic metal nanostructures as performance enhancers in emerging solar cells: A review. Next Materials, 2025. 6: p. 100509.
37. Luo, Q., et al., Plasmonic effects of metallic nanoparticles on enhancing performance of perovskite solar cells. ACS applied materials & interfaces, 2017 9(40): p. 34821-34832.
38. Ouédraogo, S., et al., Performance Enhancement Strategy of Ultra-Thin CIGS Solar Cells. American Journal of Applied Sciences, 2020. 17: p. 246-255.
39. Khadir, A., Simulation of effects of defects and layers thickness on the performance of CIGS solar cells. Acta Physica Polonica A, 2020. 137(6): p. 1128-1134.
40. Benmir, A. and M. Aida, Analytical modeling and simulation of CIGS solar cells. Energy procedia, 2013. 36: p. 618-627.
41. Mostefaoui, M., et al., Simulation of high efficiency CIGS solar cells with SCAPS-1D software. Energy Procedia, 2015. 74: p. 736-744.
42. Song, S., et al. Structure optimization for a high efficiency CIGS solar cell. in 2010 35th IEEE Photovoltaic Specialists Conference. 2010. IEEE.

ARTICLE IN PRESS